Simulation-Based Investigation of a Model for the Interaction Between Stellar Magnetospheres and Circumstellar Accretion Disks

Sean Matt

Astronomy Department, University of Washington, Seattle WA 98195

matt@astro.washington.edu

Anthony P. Goodson

Earth & Space Sciences, University of Washington, Seattle WA 98195

goodson@geophys.washington.edu

Robert M. Winglee

Earth & Space Sciences, University of Washington, Seattle WA 98195

winglee@geophys.washington.edu

and

Karl-Heinz Böhm

Astronomy Department, University of Washington, Seattle WA 98195

bohm@astro.washington.edu

ABSTRACT

We examine, parametrically, the interaction between the magnetosphere of a rotating, young stellar object (YSO) and a circumstellar accretion disk using 2.5-D (cylindrically symmetric) numerical magnetoydrodynamic simulations. The interaction drives a collimated outflow, and we find that the jet formation mechanism is robust. For variations in initial disk density of a factor of 16, variations of stellar dipole strength of a factor of 4, and for various initial conditions with respect to the disk truncation radius and the existence of a disk field, outflows with similar morphologies were consistently produced. Secondly, the system is self-regulating, where the outflow properties depend relatively weakly on the parameters above. The large scale magnetic field structure rapidly evolves

to a configuration that removes angular momentum from the disk at a rate that depends most strongly on the field and weakly on the rotation rate of the footpoints of the field in the disk and the mass outflow rate. Third, the simulated jets are episodic, with the timescale of jet outbursts identical to the timescale of magnetically induced oscillations of the inner edge of the disk. To better understand the physics controlling these disk oscillations, we present a semi-analytical model and confirm that the oscillation period is set by the spin down rate of the disk inner edge. Finally, our simulations offer strong evidence that it is indeed the interaction of the stellar magnetosphere with the disk, rather than some primordial field in the disk itself, that is responsible for the formation of jets from these systems.

Subject headings: accretion, accretion disks—ISM: jets and outflows—MHD—stars: magnetic fields—stars: pre-main sequence

1. Introduction

The formation of outflows from young stellar objects (YSO's) has been a subject of interest for some time (see summaries by Königl & Pudritz 2000; Reipurth & Bally 2001). These outflows tend to consist of a highly collimated "jet" and a poorly collimated outflow, often referred to as the "disk wind" (Kwan & Tademaru 1988, 1995). Jets have outflow velocities of $\sim$ 50 to 500 km s^{-1} and may, in some cases, exhibit spectral characteristics of a hot plasma cooling down (Bacciotti 1997). The disk wind component of the outflow typically has directionally averaged speeds of $0-50$ km s^{-1} (Hirth et al. 1997; Solf & Böhm 1993; Solf 1997) and has spectral characteristics of a cooler plasma. Some systems contain a zero velocity component, which may be due to an oblique shock interaction between the disk wind and the disk.

As observational techniques and capabilities have improved, new insights have been gained concerning the outflow properties very close to the star. For example, jet collimation can occur very close to the source star-disk system. Observations of DG Tauri using Solf's method (Solf 1989) place the collimation region within $30-40$ AU, which is the resolution of the observations of Solf & Böhm (1993). Recent measurements by Bacciotti et al. (2000) of the spatial distribution of the line emission for the Hα, [N II] 6583, [O I] 6363, and [S II] 6731 lines, at different distances from DG Tauri, imply an even closer collimation distance for this system of 14 AU. Also, Hubble Space Telescope observations of the HH 30 system (Burrows et al. 1996) imply that the jet must be fully collimated within 30 AU. For a general discussion of the collimation of YSO jets, see Eislöffel et al. (2000).

Observations of HH 30 also imply that the jet formation mechanism is episodic, producing outbursts (or "knots" along the jet axis) every ~ 2.5 years (Burrows et al. 1996). A probably related result is the observation of DG Tau by Solf (1997), who showed that the complicated [O I] 6300 line profile from the immediate environment of DG Tau changes drastically within 1 year. Larger scale observations of other systems such as HH 111 imply a knot ejection timescale of ~ 15 years (Reipurth et al. 1992), but there is no consensus as to whether or not the timescales of HH 30 and HH 111 are due to the same physical principle.

One result of so many recent observational insights is that significant progress has been made in understanding the mechanism which generates YSO outflows. While hydrodynamic means have been investigated (e.g., a stellar wind which is collimated via shock focusing; see, e.g., the early paper by Königl 1982; Frank & Mellema 1996), the models that have met the most success have relied on magnetic fields to launch and collimate the outflow. These models fall into two categories: those that rely solely on a magnetic field which threads the disk to centrifugally fling the wind (and eventually collimate into a jet; see, e.g., Pudritz & Ouyed 1997; Camenzind 1997; Kuwabara et al. 2000), and those that depend on the interaction between the stellar magnetic field and the accretion disk (e.g., Lovelace et al. 1995, 1999; Hayashi et al. 1996; Miller & Stone 1997; Goodson et al. 1997, 1999; Goodson & Winglee 1999). In the model of Goodson et al. (1997, henceforth GWB), Goodson et al. (1999, henceforth GBW), and Goodson & Winglee (1999, henceforth GW), a stellar dipole field couples the star to the disk, differential rotation between the star and the disk rapidly inflates the magnetic field via helicity injection, and an outflow burst is produced with both jet and disk wind properties. Magnetic reconnection allows the process to repeat. Hayashi et al. (1996) and GWB identified this basic mechanism within a few stellar radii, and GBW illustrated the resulting outflow out to several AU with a magnetohydrodynamic (MHD) simulation in a single case study. GW laid out some of the physics driving key characteristics of the outflow and star-disk interaction, allowing some predictions to be made beyond their case study.

The work presented in GBW and GW implied that the interaction between the stellar magnetosphere and the innermost regions of the accretion disk could produce an outflow that is qualitatively similar to those observed. The outflow consists of a knotty jet (collimated within 1 AU) that is morphologically similar to the observations of HH 30 (Burrows et al. 1996). However, the size scale is an order of magnitude smaller than HH 30, and the timescale for knot formation is an order of magnitude shorter. In addition to the apparent mismatch between observation and simulation results, issues that must be addressed are:

1. The dipole field from the star initially threads the disk everywhere. Thus, it is not clear if the outflow is a result of the interaction between the star and the disk (as claimed in

GW), or if it is due to the magnetic field which threads the disk everywhere at $t = 0$.

2. The results of GBW represent a single case study. The sensitivity of the jet formation mechanism to key attributes of the star-disk system was not directly established.

To address these issues, we repeated the basic simulation of GBW for various disk densities, stellar magnetic field strengths, and magnetic field configurations. Section 2 contains the details of the parametric cases and of the outflows that result in each case. The parametric simulations also allow us to evaluate the disk oscillation model of GW in §3. A semi-analytical approach, including a formulation of the extraction of angular momentum from the disk, leads to a modification and enables testing of the modified model. A summary and discussion follows, in §4.

2. Simulations and Outflow Results

We used the 2.5-D (axisymmetric) MHD simulation code employed by GWB, GBW, and GW to examine, parametrically, the effect of varying the accretion disk density, the stellar dipole field strength, and the initial magnetic field configuration. The simulation code employs a two-step Lax-Wendroff (finite difference) scheme (Richtmyer & Morton 1967) to simultaneously solve the following time-dependent, MHD equations:

$$\frac{\partial \rho}{\partial t} = -\boldsymbol{\nabla} \cdot (\rho \boldsymbol{v}) \tag{1}$$

$$\rho \frac{\partial (\boldsymbol{v})}{\partial t} = -\rho (\boldsymbol{v} \cdot \boldsymbol{\nabla}) \boldsymbol{v} - \boldsymbol{\nabla} P - \frac{GM_* \rho}{(\boldsymbol{r}^2 + \boldsymbol{z}^2)} \hat{\boldsymbol{R}} + \frac{1}{c} (\boldsymbol{J} \times \boldsymbol{B}) \tag{2}$$

$$\frac{\partial e}{\partial t} = -\boldsymbol{\nabla} \cdot [\boldsymbol{v}(e + P)] - \left[\frac{GM_* \rho}{(\boldsymbol{r}^2 + \boldsymbol{z}^2)} \hat{\boldsymbol{R}} \right] \cdot \boldsymbol{v} + \boldsymbol{J} \cdot \boldsymbol{E} \tag{3}$$

$$\frac{\partial \boldsymbol{B}}{\partial t} = -c (\boldsymbol{\nabla} \times \boldsymbol{E}) \tag{4}$$

and uses

$$\boldsymbol{E} = -\frac{1}{c} (\boldsymbol{v} \times \boldsymbol{B}) + \eta \boldsymbol{J} \tag{5}$$

$$\boldsymbol{J} = \frac{c}{4\pi} (\boldsymbol{\nabla} \times \boldsymbol{B}) \tag{6}$$

$$e = \frac{1}{2} \rho |\boldsymbol{v}|^2 + \frac{P}{\gamma - 1} \tag{7}$$

where ρ is the density, $\boldsymbol{v}$ the velocity, P the scalar gas pressure, e the internal energy density, $\boldsymbol{B}$ the magnetic field, $\boldsymbol{J}$ the volume current, $\boldsymbol{E}$ the electric field, c the speed of light, and γ

the ratio of specific heats (we used $\gamma = 5/3$ in our simulations). In the momentum and energy equations (2 and 3), we include a source term for gravity in which G is the gravitational constant, M_* is the stellar mass, r and z are the usual cylindrical coordinates, and R is the spherical distance from the center of the star ($|R|^2 = |r|^2 + |z|^2$). The last term in equation 5 allows us to explicitly model the Ohmic diffusion of the magnetic field by specifying the value of the resistivity, η. As discussed by GW, the numerical diffusivity intrinsic to the simulations is measured to be $\approx 5 \times 10^{16}$ cm^2 s^{-1}. In order to properly capture the physics of magnetic diffusion, we use $\eta = 10^{17}$ cm^2 s^{-1} in all of our simulations.

We use a "nested box" scheme, and for the work presented here, all simulations used 5 nested boxes, each with half the resolution (and so twice the physical size) as the one interior to it. Each box consists of a 401×100 (in the cylindrical r and z direction, respectively) grid. As in GBW and GW, the grid spacing is 0.1 $R_\odot$ in the innermost box, but the outermost box dimensions are 3.2 AU by 0.8 AU. The innermost (in R) boundary consists of a 15 gridpoint sphere (the "surface of the star"), where ρ, P, B, and v are held fixed at the initial values. We enforce reflection symmetry across the equatorial plane. Along the rotation axis, we require that $B_\phi = B_r = v_\phi = v_r = 0$, and all other quantities are equal to the value at $r = dr$ (where dr is the grid spacing). We adopt outflow conditions (the spatial derivative across the boundary is zero for all quantities) at the outermost boundary of the outermost box.

The initial conditions for the baseline case of this study is parametrically identical to the case illustrated by GBW. They describe the initial conditions for this case in considerable detail (see their table 1), which includes a disk similar to a classic α model accretion disk (Shakura & Sunyaev 1973) with $\dot{M}_{\rm acc} = 10^{-7}$ $M_\odot$ yr^{-1} and $\alpha = 0.2$ $(r_{\rm au})^{-1.5}$ (where $r_{\rm au}$ is the usual cylindrical coordinate in units of AU). The stellar magnetic field is dipolar, with a field strength of 1800 G at the pole of the 1 $M_\odot$, 1.5 $R_\odot$ central star. Initially, the stellar corona is in hydrostatic equilibrium, and the density falls of as R^{-4}. The star rotates with a period of 1.8 days (which is fairly close to the shortest observed rotation period of CTTS; see, e.g., Bouvier et al. 1986), and the disk is initially truncated at 8.5 $R_\odot$ and has a midplane density of 2.2×10^{-10} g cm^{-3} at 10 $R_\odot$. The dipole field threads the disk everywhere at the start of the simulation.

To save computational time, this work focuses more on the outflow generation mechanism and the integrated outflow properties instead of the larger scale outflow morphology. The simulation cases were all carried out for a period of at least 160 days of real time (requiring 30-60 days of computing time per case).

Table 1 serves as a quick reference for all simulation cases in this study. The three cases which examine variations of initial disk density are the "low density," "baseline," and "high density" cases. The three which examine variations of stellar field strength are the "weak

field," "baseline," and "strong field" cases. The relative factors by which the disk density and the magnetic field strength were varied were chosen based on energy balance. This is because the importance of the magnetic field is measured by the ratio of the magnetic energy to the kinetic energy in the disk. Since the disk kinetic energy is proportional to the disk density, and the magnetic energy scales as the square of the stellar field strength, we varied the initial disk density by factors of 4 and the initial magnetic field strength by factors of 2.

We also investigated simulations with a "primordial," vertical magnetic field in the disk. So that the stellar magnetosphere was truncated (at the region of disk and stellar field equality) near the star, the simulations use stellar dipole strength equal to the weak field case, plus a vertical field of 0.07 Gauss everywhere in the simulation region. These parameters give a stellar magnetosphere that is truncated at 29 $R_\odot$ in the equatorial plane. The stellar magnetosphere has an open or closed topology, depending on the polarity of the primordial field. The vertical field in these simulations cases is relatively weak (in that the stellar dipole is dominant for an extended region; the ratio of magnetic to kinetic energy near the disk inner edge is $\sim 10^{-5}$) but is sufficient to assess the effect of the dipole field that initially threads the disk at all radii in the other cases. In order to initially exclude the disk from the stellar magnetosphere, we truncated the disk at 29 $R_\odot$ for these models. Therefore, our models with various magnetic field topologies comprise three cases: One with a downward-directed ($-z$) vertical field ("closed magnetosphere"), one without a vertical field ("truncated disk"), and one with an upward-directed field ("open magnetosphere"). All three have a stellar dipole field with the same strength as the weak field case, and all have a disk truncation radius at 29 $R_\odot$ (which is 3.4 times further out than all the other simulations).

2.1. Outflow Morphology

Figures 1 – 3 illustrate the general outflow morphology for all cases. In these figures, the density grayscale (logarithmic) and poloidal velocity vectors represent data in the outermost box for a single "snapshot" in time. Data from the inner 100×100 grid points of the outer box are shown, reflected about the rotation axis to better show the jet. The grayscale emphasizes material in the outflow, but does not capture the relatively high density distribution near the star and disk inner edge. For a detailed look at the complex and time-dependent density distribution near the star, see figures 3 and 4 of GBW. Note that different times are represented for each case. This is because the launching mechanism is essentially periodic, with the period being different for each case. The innermost regions of the disk oscillate radially, and each oscillation triggers a large scale reconnection event which alters the shape

of the outflow in a periodic way. For the purpose of comparison, we show the various cases at a similar phase (but not at the same time) of their outflow.

As evident in figure 1, disk density variations of a factor of 16 have no major effect on the outflow morphology. The basic outflow, in all cases, consists of a wide angle component (the "disk wind") and a jet. Also note that even at this close-in scale (on the order of an AU), the general characteristics of both the jets and disk winds are similar – knots in the jet are apparent in each case (most clearly in the high-density case), as are the "wispy" structures between the disk and jet (associated with magnetic reconnection; see GBW).

While the general morphologies are remarkably similar, some differences between the outflows in figure 1 are apparent. The low density case has a higher outflow speed, a lower outflow density, and a larger spacing between knots in the jet that the other cases. Conversely, the high density disk case has a higher density, slower outflow, and the spacing between the knots in the jet is reduced considerably. This reduction in knot formation period is related to a reduction in the period of radial disk oscillations (discussed further in §3).

Figure 2 represents the simulation cases which examined variations in stellar magnetic field strength. Again, the morphologies of all runs are similar, indicating that variations of a factor of 4 in magnetic field strength produce no significant variation in large scale morphology. Each outflow produces a knotty jet with a disk wind and a wispy structure in the region between the disk and jet. However, differences between the outflows in figure 2 are evident. The outflow is slower in the weak field case and faster in the strong field case. Also, the structure of the disk wind in the weak field case has a more complicated appearance than the other two cases.

Figure 3 illustrates the outflows for the cases with different large scale magnetic field topologies. Insets in each of the three panels show the topology in the initial conditions. Once again, note that the general morphologies of the outflow are all similar. Recalling from table 1 that these three topologies are variants of the weak field case, it is interesting to note that all of these cases exhibit the same general characteristics of the weak field case (fig. 2). All produce outflows with jets and disk winds (including wispy structures) with velocities similar to the weak field case, and all three cases in figure 3 produce outflows with a complicated structure (relative to the other cases) on the one AU scale. This figure is particularly noteworthy because, in the bottom two panels, the disk is threaded everywhere by a vertical field, so it has much more magnetic energy in the disk (at large radii) than the cases with only a stellar dipole. The fact that the outflows in these cases are not significantly different from the top panel, supports the underlying premise of the model: It is the interaction between the stellar magnetosphere and the surrounding accretion disk that produces the outflow, and the effect of the dipole field lines initially threading the disk at

large radii is insignificant.

The primary conclusion to be drawn from figures 1 - 3 is that the outflow formation mechanism is robust. Also, to the extent these parameters were varied, the jet morphology produced by this mechanism is independent of the density of the accretion disk, the strength of the stellar magnetic field, and the large scale magnetic field topology. As seen in these figures, however, the magnitude and timescales of outflow characteristics do depend on the magnetic field strength and the density of the accretion disk, and the remainder of this paper addresses these dependencies in a quantitative way.

2.2.   Sensitivity of Outflow Properties

Figure 4 shows the variation in radial outflow velocities for all cases. For the data in this figure we first calculated the radial velocity ($\boldsymbol{v} \cdot \hat{\boldsymbol{R}}$) on a sphere with a radius of 0.67 AU (90 grid points in the outer box) centered on the star. Due to the periodic nature of the system, and because we were most interested in the global outflow properties, we used a time average value. Since it takes a while for the outflow to clear out the entire simulation region, our average only includes data from the interval of 50 – 160 days. We thus obtain the average velocity as a function of angle from the pole. The data in figure 4 represent the maximum of the time-averaged velocity, which occurred at ~ 40 degrees for all cases. The leftmost panel shows the velocities as a function of the disk variation, the middle as a function of the initial magnetic field energy, and the right panel as a function of the vertical field strength. Note that the entire range of velocities (100 to 200 km s^{-1}) is well within the range of observed outflow velocities (50 to 500 km s^{-1}) and corresponds to the velocities in most of the observed HH objects (see Raga et al. 1996).

In panel a), the radial outflow velocity decreases with increasing disk density, while in b), the outflow velocity increases with increasing magnetic field energy. Finally, panel c) shows that the outflow velocity is roughly independent of the large-scale magnetic field topology. It is important to note that the velocities in panel c) are similar to the weak field case. Remember that the simulations represented in c) have their disk initially truncated 3.3 times further out than the weak field case, and two of them have an additional vertical "primordial" field. We see from panel b) that the outflow velocity depends on the magnetic energy (from the stellar dipole), so the fact that panel c) shows essentially no trend suggests that it is only the magnetic energy in the stellar magnetosphere that is important for accelerating the outflow.

The data in panels a) and b) can be fit with a power law ($v_{\rm w} \propto \rho_{\rm d}^n$ and $v_{\rm w} \propto E_{\rm mag}^n$,

respectively, where ρ_d is the initial disk density and E_mag is the initial magnetic energy associated with the stellar dipole field). A least squares minimization fit gives $n = -0.2$ and 0.3 for panel a) and b), respectively. We note that there is not necessarily a physical justification for fitting all of the data with a power law, but we will use it to quantify the dependence of various system properties on the parameters we varied.

Figure 5 shows the variation in mass outflow rates, $\dot{M}_\mathrm{w}$, for the three parametric studies. To obtain these points (and the ones for L_w and $\dot{J}_\mathrm{w}$, discussed below), we first calculated the mass flux (also energy flux and angular momentum flux) through a sphere at 0.67 AU. The mass outflow rate (also L_w and $\dot{J}_\mathrm{w}$) is given by an integration over the surface of the sphere and a time average over the interval of 50 – 160 days. In an effort to exclude the disk (which can be inflowing or outflowing, but with very high mass relative to the jet and disk wind), the data shown represent an integration over the surface up to an opening angle of 75 degrees. To get an idea of the relative uncertainties (due to the fact that we are representing a time-dependent property by a time-averaged value) in the data, we calculated the cumulative average of $\dot{M}_\mathrm{w}$ during the 50 – 160 day interval. We take three times the standard deviation of this cumulative average over the interval of 85 – 160 days as our uncertainty. This quantity reflects the uncertainty due to the periodicity of $\dot{M}_\mathrm{w}$ and due to the settling down of the system to a fixed period (discussed further in §3).

All of the data in figure 5 have $\dot{M}_\mathrm{w} \sim 10^{-7} - 10^{-8}\ M_\odot\ \mathrm{yr}^{-1}$, consistent with observations of YSO outflows (Hartmann 1997). Also, $\dot{M}_\mathrm{w}$ increases with both disk density and magnetic field energy. Once again, a power law nicely quantifies this dependence with $n = 0.2$ for both panel a) and b) (within uncertainty). The variation of mass outflow rate with the different field topologies, panel c), shows no clear trend.

Figure 6 shows the variation in outflow luminosity, L_w, for the parametric cases studied. The energy flux is the sum of the kinetic, magnetic, and the thermal energy fluxes.

$$\Phi_\mathrm{eng} = \left(\frac{1}{2}\rho v^2 + \frac{P}{\gamma - 1} + \frac{B^2}{8\pi} \right) (\boldsymbol{v} \cdot \hat{\boldsymbol{R}}), \tag{8}$$

and the data in figure 6 represent the time-averaged, integrated flux (as for $\dot{M}_\mathrm{w}$ above). The format of the figure is the same as figures 4 and 5. The disk density has no obvious influence on L_w, and the best fit power law is consistent with $n = 0$. The outflow luminosity does, however, depend on the initial magnetic field energy, suggesting a power law with $n = 0.4$. Finally, the addition of a weak vertical field has no significant impact on outflow luminosity.

An analysis of the angular momentum carried in the outflow, $\dot{J}_\mathrm{w}$, is deferred to §3.1, where we use a semi-analytical formulation to understand the controlling parameters of the angular momentum extracted from the inner edge of the accretion disk.

2.3. Large Scale Magnetic Field Evolution

In the jet launching process described in GBW (also in Hayashi et al. 1996, and, to some degree, in Lovelace et al. 1999), the large scale magnetic field undergoes rapid inflation. This inflation results from the differential rotation between the star and the disk which twists the magnetic field, injecting helicity, and increasing the overall magnetic energy. The resulting magnetic field has characteristics that differ significantly from those of a dipole. Figure 7 illustrates the initial magnetic field expansion of the baseline case, demonstrating the rapid change from a dipole to a more complicated and open geometry.

The basic process of magnetospheric inflation can be summarized as follows (see GWB and GBW for details): The star is initially connected to the disk via the dipole magnetic field. Differential rotation between the star and disk induces an azimuthal component of the magnetic field, increasing the magnetic pressure ($|\boldsymbol{B}|^2/8\pi$) in the twisted region, which in turn inflates the poloidal component of the magnetic field.

The expanded magnetic field has many properties that are different from the simple dipole. Figure 8 illustrates the most significant differences for the discussion at hand. The figure shows the total magnetic field strength, $|\boldsymbol{B}|$, on a 45 degree line in the meridional plane for the baseline case. The lower solid line shows the original dipole field. The top solid line shows the total field, $|\boldsymbol{B}|(\mathrm{tot}) = (B_r^2 + B_\phi^2 + B_z^2)^{1/2}$, and the middle solid line shows the poloidal field, $|\boldsymbol{B}|(\mathrm{pol}) = (B_r^2 + B_z^2)^{1/2}$, both at $t = 61.6$ days.

Note that the dipole field decreases with distance as R^{-3}, the evolved total field decreases as R^{-n} with n near 1.7, and the evolved poloidal field decreases with n roughly equal to 2.0. Also note that the evolved field has a "dipole-like" ($n \sim 3$) region close to the star ($R \lesssim 5R_\odot$), with a clear transition to an "expansion-dominated" ($n \sim 1.5$-2) region beyond. The total and poloidal field strengths are almost identical in the dipole-like region, indicating that B_ϕ is negligible there. A piece-wise continuous fit was made of the expanded field (along a 45° slice), of the form:

$$|\boldsymbol{B}| = \mathrm{Max}\left[B_{01}\left(\frac{R_*}{R}\right)^{n_1}, B_{02}\left(\frac{R_*}{R}\right)^{n_2}\right] \tag{9}$$

In this fit, n_1 is the power law that applies in the interior, dipole-like region, and n_2 is the power law that applies in the exterior, expanded region. B_{01} and B_{02} are the field strengths that one would obtain at the surface of the star, if the power law could be extrapolated all the way to the stellar surface (this is roughly the true surface value for the dipole-like fit, but not for the expanded field fit). Both the total and poloidal field are fit in this way. The dashed lines in figure 8 are the fits to the total and poloidal field at $t = 61.6$ days.

Table 2 lists the values of the magnetic field fit parameters for all of the simulations.

Since the values are time-dependent (periodic), and it takes some time for the flow to be established in the entire simulation grid, table 2 data have been averaged during the interval of 50 – 160 days. To get an idea of the uncertainty of these values (due to the episodic nature of the system), we first obtain the cumulative average during this interval. The uncertainty listed in the table is the standard deviation of this cumulative average during the interval of 85 – 160 days. For each case, column 2 and 3 contain the B_{01} (in Gauss) and n_1 values. Since the total and poloidal field is nearly identical in this interior fit, we list only the value for the poloidal field. The last 4 columns contain similar values for the exterior portion of the fit for both the total and poloidal field components.

When $n_2(\mathrm{pol})$ is near 2.0, the poloidal field is essentially open ($n = 2$ for a purely radial field). This is roughly true for all cases, though the ones with weaker dipole fields (row 4 and 6 – 8) have $n_2(\mathrm{pol})$ significantly less than than 2. The primary conclusion from this data is that the total magnetic field strength will behave as R^{-n} where n is between 1.5 and 2.0. The cases with additional vertical field in the disk (last two rows of table 2) have the largest magnetic to kinetic energy ratios (far from the disk inner edge) of all cases. However, since the magnetic field in the outflow originates in the stellar magnetosphere, the field in the evolved outflow of these cases is identical to the weak field and truncated disk case.

2.4. Summary of Parametric Results

The most striking result of this parametric study is that every case examined produces an outflow similar to that of GBW. For a variation of disk density of a factor of 16, a variation in stellar magnetic field of a factor of 4, and variations in initial disk truncation points and large scale magnetic field topologies, all of the simulations produce outflows with jets and disk winds. The only differences are in the details of the star-disk interaction and in the magnitude of the outflow properties.

Table 3 summarizes the sensitivities of the outflow properties and morphology to increasing the disk density and increasing the stellar magnetic energy. The listed numerical values are the spectral index (n) from power laws that represent various data (e.g., the dotted lines in figures 4 - 6). The least squares power law fits were weighted by the uncertainty (as described in §2.2), and the errors in table 3 are the formal 1-sigma errors of the fit. Note that some of outflow properties listed in table 3 are discussed in the following section.

The main result of table 3 is that variation of key system parameters do indeed cause variations in outflow properties, but the relationship is weak (i.e., $|n|$ is small). The star-disk-field system is self-regulating, due to the interaction between the disk and the outflow.

The system adjusts to mitigate the impact of any single parameter change. Also, the large scale field topology does not significantly affect any of the outflow properties. This result implies that it is indeed the interaction between the stellar magnetosphere and the accretion disk that drives the outflow, as opposed to the existence (via artificial initial conditions as in GBW) of a dipole field that threads the disk everywhere at $t = 0$.

3. Evaluation of the Disk Oscillation Model of GW

As noted in GBW and GW, the inner edge of the disk undergoes radial oscillations. These oscillations are actually a flux exchange process – on each oscillation, the stellar magnetosphere diffuses into the innermost regions of the disk and differential rotation inflates the magnetic field to an open configuration. The inflated field topology spins the disk down via magnetocentrifugal launching of disk plasma (see, e.g., Blandford & Payne 1982). As it spins down and moves inward toward the star, the disk inner edge is stripped away from the rest of the disk. At the point of "closest approach", a reconnection event alters the magnetic field topology, and the spun down portion of the disk flows along the newly reconnected field lines, accreting onto the star.

Figure 9 illustrates the disk oscillations for the simulation cases where the accretion disk density is varied. The solid line is the radial location of the inner edge of the disk as a function of time. The dashed line shows the location of the Keplerian co-rotation point (where the stellar solid body rotation rate is equal to the Keplerian rotation rate). The figure clearly demonstrates the dependence of disk oscillations on the disk density. As disk density is decreased, the amplitude and period of the oscillations increase. Note that it takes time for the system to settle down to a constant period (the physical explanation for this is discussed in §3.2). In most cases, the system becomes quasi-periodic after about 50 days, but the low density case seems only to be settling down near the end of the 160 day simulation. Much of our uncertainty in all quantities is due to this effect, and we have calculated our uncertainties to reflect this.

As the average disk location approaches the Keplerian co-rotation point, the difference between the disk and stellar magnetosphere rotation rates is reduced, so the magnetosphere will expand more slowly. This is true in the high density case (bottom panel), but here the disk oscillations are actually faster than in the other cases. Also, even in the high density case, the oscillation period is much longer than the inflation timescale (which is roughly the time for the disk inner edge and star to rotate to a differential angle of π; see Uzdensky 2002; GW). This supports the basic tenet of GW that the oscillation period is driven by the spin-down rate of the inner edge of the disk (via magnetic torques) rather than the inflation

rate of the magnetic field.

Ideally, the parametric simulation results presented here would allow for the disk oscillation model of GW to be tested. Unfortunately, the data in §2.3 require us to relax their assumption that the expanded magnetic field has reached a power law configuration characterized by $|\boldsymbol{B}| = B_*(R_*/R)^2$. While this may be true for the poloidal field of many cases (see table 2), it is more generally true that the expanded field reaches a configuration with $|\boldsymbol{B}| = B_0(R_*/R)^n$, with n between 1.5 and 2.0 (and B_0 not necessarily equal to the stellar surface value). We will also discard the assumption of GW that the accretion disk has reached a secular steady state, where the accretion rate onto the star (regulated by the interaction between the stellar magnetosphere and the inner edge of the disk) equals the accretion rate given by the α-disk description of the disk. While this secular steady state does exist near the end of simulations, the accretion rate in the outer portion of the simulated disk is unlikely to be equal to the α-disk model. This is because the physics of the Shakura-Sunyaev α-disk model are not fully captured in the simulations. However, we will show in the following section that the extraction of angular momentum from the inner edge of the disk can be simply understood and determined from simulation data. In light of this, we present a modified disk oscillation model (in §3.2), in which the angular momentum extraction can be a prescribed value – thus removing the assumption of secular stead state in the disk.

We should point out that it is our ultimate goal to be able to determine the properties of the outflow ($\dot{M}_{\rm w}$, $v_{\rm w}$, $L_{\rm w}$, oscillation period, etc.) generated by the star-disk interaction a priori from the physical parameters of the system (R_*, B_*, disk accretion rate, etc.). Unfortunately, the complexity of the model, which includes a relatively large number of parameters, makes this difficult. The following work in this section is thus meant to be an early step in that direction. As such, this semi-analytical work relies on some quantities derived from the outcome of the simulations (e.g., B_0). The work presented in §3.1 and §3.2, therefore, is useful for testing our understanding of the most relevant physics controlling the oscillations, and thus the accretion/ejection mechanism. It will also serve as a check for self-consistency in the simulations.

3.1. Extraction of Angular Momentum from the Disk

Consider an inner region of the disk that is threaded by a magnetic field. From the analytical work of Weber & Davis (1967), we note that the angular momentum transported in the wind of a magnetic rotator is $\dot{J}_{\rm w} = \dot{M}_{\rm w}\Omega_{\rm fp}R_{\rm A}^2$ (where $\Omega_{\rm fp}$ is the angular velocity of the footpoint of the flux tube, and $R_{\rm A}$ is the Alfvèn radius). Assuming nearly rigid rotation

of plasma out to R_A (for a discussion of this assumption, see, e.g., Michel 1969), plasma will be magnetocentrifugally launched along field lines via the Blandford-Payne mechanism (Blandford & Payne 1982), provided the field lines make an angle of more than 30 degrees from vertical. This angle is typically 45 to 55 degrees in our simulations. For a simple approach, we'll assume that the velocity of the wind at the Alfvèn radius is $v_{R_A} = \Omega_{\rm fp} R_A$. This is strictly true for $R_A \gg R_{\rm d}$ (where $R_{\rm d}$ is the position of the field footpoint in the disk). The Alfvèn radius, then, can be estimated by examining the energy balance at that location:

$$\frac{1}{2}\rho_{R_A} v_{R_A}^2 = \frac{B_{R_A}^2}{8\pi}, \tag{10}$$

When expressed in terms of outflow properties, and assuming the magnetic field behaves as $|\boldsymbol{B}| = B_0(R_*/R)^n$, this becomes

$$\frac{1}{2}\frac{\dot{M}_{\rm w}\Omega_{\rm fp}}{4\pi f R_A} = \frac{B_0^2}{8\pi}\left(\frac{R_*}{R_A}\right)^{2n} \tag{11}$$

Here, we have assumed that $\dot{M}_{\rm w} = 4\pi R_A^2 \rho_{R_A} v_{R_A}$. Note that this assumption is not valid for an anisotropic wind, so we introduced a filling factor, f, by which the mass outflow rate is reduced. Reducing equation 11 and solving for R_A gives

$$R_A = \left(\frac{f B_0^2 R_*^{2n}}{\dot{M}_{\rm w}\Omega_{\rm fp}}\right)^{\frac{1}{2n-1}} \tag{12}$$

and so

$$\dot{J}_{\rm w} = (\dot{M}_{\rm w}\Omega_{\rm fp})^{1-\frac{2}{2n-1}}(f B_0^2 R_*^{2n})^{\frac{2}{2n-1}} \tag{13}$$

The dependence of $\dot{J}_{\rm w}$ on various outflow properties is interesting. The strength of the dependence relies only on n, the magnetic field power law fall off. Note that if $n = 1.5$, equation 13 becomes

$$\dot{J}_{\rm w} = f B_0^2 R_*^3, \tag{14}$$

and $\dot{J}_{\rm w}$ is independent of both $\dot{M}_{\rm w}$ and $\Omega_{\rm fp}$. In general, for any n between 1.5 and 2.0, the exponent on the factor $(\dot{M}_{\rm w}\Omega_{\rm fp})$ in equation 13 is substantially smaller than on the factor $(f B_0^2 R_*^{2n})$. Therefore, the extraction of angular momentum should be most sensitive to the magnetic field strength.

The simulations verify this conclusion. Figure 10 shows the angular momentum outflow rate for all cases. The data (squares) are calculated as described in §2.2, and shown in the same format as figure 4. It is clear that the angular momentum carried in the simulation outflow is more dependent on magnetic energy than on disk density, which influences $\dot{M}_{\rm w}$

and $\Omega_{\rm fp}$ (see figures 5 and 9). In fact, panel a) of figure 10 shows no obvious dependence of $\dot{J}_{\rm w}$ on disk density at all (also see the fifth row of table 3). This also appears to be true for the cases with various field topologies shown in panel c), where there is no clear trend, especially considering the larger uncertainties.

The simulations also offer a quantitative test of equation 13. We used the time-averaged simulation values for $\dot{M}_{\rm w}$, $\Omega_{\rm fp}$, B_0, and n (the magnetic field power law fall off) for each case and calculated $\dot{J}_{\rm w}$ using equation 13. Since the inner edge of the disk spends most of the time beyond 5 $R_\odot$ (see figure 9), the value of B_0 and n to use comes from the outer portion of the piece-wise fit to the magnetic field strength in the simulations. Also, since angular momentum is added to the wind via the poloidal field anchored in the disk, the calculated values of $\dot{J}_{\rm w}$ use $B_{02}({\rm pol})$ and $n_2({\rm pol})$. We chose a single value of the filling factor ($f = 0.43$), so that the calculated values match the baseline result. These calculated values (triangles in figure 10) can be directly compared to the simulated values (squares), and the agreement between them is remarkable. The largest disagreement is (for the closed magnetosphere case) at the 50% level.

In the context of equation 13 and the assumptions at the beginning of this section, it seems clear that variations in the location of the inner edge of the disk (which is the launching point for much of the outflow) and in $\dot{M}_{\rm w}$ (which is related to the conditions at the footpoint of the flux tube) have little relative impact on the angular momentum ejected from the system. The primary reason for this is the restructuring of the initial magnetic field. As evident in table 2 (also see figs 7 and 8), the magnetic field rapidly evolves into a state that follows a radial power law with n between 1.5 and 2.0, increasing the importance of B_0 relative to $\dot{M}_{\rm w}$ and $\Omega_{\rm fp}$.

In addition to this, the magnetic field in the outflow seems to be restructured in such a way that it "softens" the effect (on $\dot{J}_{\rm w}$) of the parameters varied. For example, the $B_{02}({\rm tot})$ values for the weak field, baseline, and strong field cases are 550, 750, and 1180 Gauss, respectively. The entire range in these values is only a factor of 2, even though the entire range of stellar surface dipole field strengths (which is the only simulation parameter changed among these cases) is a factor of 4. Thus, a given variation in the stellar surface magnetic field strength cannot be used in conjunction with equation 13 alone to determine the resulting variation in $\dot{J}_{\rm w}$. The self-regulating nature of the system indeed makes prediction difficult.

3.2. Modified Disk Oscillation Model

In their oscillation model, GW assumed that the magnetic field associated with the stellar magnetosphere would diffuse into the disk radially at a given radial velocity (v_{diff}). The differing azimuthal velocities of the inner edge of the disk and the stellar magnetosphere (which rotates at the angular rotation rate of the star) leads to a rapid inflation of the magnetosphere (note that $v_\phi \gg v_r$ and v_{diff}). The inflated magnetic configuration removes angular momentum from the inner edge of the disk (via magnetocentrifugal launching of disk plasma), spinning it down. The inner edge of the disk will eventually achieve the condition where its inward radial velocity exceeds the velocity at which the magnetic field is diffusing out into the disk ($|v_r| \gtrsim |v_{\mathrm{diff}}|$). At this point, the inner edge of the disk separates from the rest of the disk, and spirals inward to the star, where a fraction of it is ultimately accreted by the star, and a fraction is expelled in the outflow. Thus, the diffusive velocity (v_{diff}) determines how much of the disk separates for each oscillation, and so sets the mass accretion rate.

There are two main assumptions in the disk oscillation model of GW that must be modified. They calculated the radial velocity of the disk inner edge (as it spins down; their eq. 9) as a function of r, v_{diff}, R_{d} (the radial position of the disk inner edge), $\Sigma(R_{\mathrm{d}})$ (the surface density there), and B_*. We first modify their assumption that $|\boldsymbol{B}| = B_*(R_*/R)^2$ to the more general case, $|\boldsymbol{B}| = B_0(R_*/R)^n$, and get

$$v_r = -B_0^2 R_*^{2n} r^{2-2n} \frac{\{GM_*[2\pi R_{\mathrm{d}}\Sigma(R_{\mathrm{d}})]^2 r - B_0^2 R_*^{2n}\pi R_{\mathrm{d}}\Sigma(R_{\mathrm{d}})r^{4-2n}\}^{\frac{1}{2}}}{GM_*[2\pi R_{\mathrm{d}}\Sigma(R_{\mathrm{d}})]^2 - B_0^2 R_*^{2n}\pi R_{\mathrm{d}}\Sigma(R_{\mathrm{d}})(4-2n)r^{3-2n}} \tag{15}$$

Note that when $n = 2$, equation 15 reduces to GW's equation 9.

The second assumption of GW to discard is that the accretion rate from the disk inner edge (regulated by the interaction of star's magnetosphere and the disk) is the same as the accretion rate given analytically by the α-disk description. Instead, we assume that the angular momentum carried in the outflow (see §3.1 and fig. 10) is equal to the amount extracted from the disk inner edge.

Figures 11 and 12 contain the simulated disk oscillation amplitudes and periods (squares and dotted lines; in the same format as fig. 4). Since it takes some time for the oscillations to settle down (see fig. 9), the simulated amplitude of the disk oscillations plotted in figure 11 are the maximum separation of the star and disk inner edge 160 days into the simulation. The simulated periods (fig. 12) are also taken at this time. As a measure of the uncertainty (represented by error bars in the figures), we use the difference between the amplitude at 160 days and the value at 85 days. For the period, we use the same method, but the error bars have been doubled to show up better on the plot.

The "settling down" of the disk oscillations is a result of the initial conditions. Equation 15 indicates that, as R_{d} increases, v_r decreases (due to a decrease in the magnetic torque and an increase of the amount of angular momentum at that radius), and a ring from the disk inner edge has further to fall, so the period increases. Also, GW showed (their fig. 7) that the accretion rate decreases for increasing R_{d}. If the initial state of the system (in the simulations) is such that the accretion rate regulated by the star-disk interaction ($\dot{M}_{\mathrm{inner}}$) is greater than the accretion rate further out in the disk (at $r > R_{\mathrm{d}}$; $\dot{M}_{\mathrm{outer}}$), the inner region of the disk will be cleared out (thus increasing R_{d}) until the two accretion rates are equal.

Notice that the cases in panels a) of figures 11 and 12 show a relatively strong variation in amplitude and period, even though the angular momentum extraction rate is roughly equal among them (see fig. 10). This is explained by the fact that, for a denser disk, $\dot{M}_{\mathrm{outer}}$ is larger, so the final state of the system will have a smaller amplitude and, therefore, a shorter period.

The previous section showed that angular momentum extraction depends most strongly on the magnetic field strength. This seems to imply that, for stronger magnetic fields, the oscillation periods should be shorter (since a ring of disk material would spiral in faster). This would indeed be the case if R_{d} were a fixed quantity. However, when the magnetosphere-disk interaction can extract more angular momentum from a given radius, $\dot{M}_{\mathrm{inner}}$ increases, so the final state of the system will actually have a larger R_{d} and a longer period. This is evident in panels b) of figures 10 – 12.

To calculate the period and amplitude of disk oscillations, following GW, we used an iterative process in which we first pick a radial location for the disk inner edge (R_{d}) and integrate equation 15 to obtain a spin down time. Equation 15 requires the case-specific values of $B_{02}(\mathrm{tot})$ and $n_2(\mathrm{tot})$ listed in table 2. This method gives a simultaneous prediction of the oscillation amplitude and period. As opposed to GW, we adopt the R_{d} value that satisfies the requirement that the angular momentum extracted from the ring of material (as it falls toward the star) divided by the oscillation period (taken as twice the spin down time) equals the angular momentum extraction rate in the simulations (displayed in fig. 10). As in GW, we need an estimate of v_{diff}, in order to calculate the mass of the ring of material that is stripped off of the disk inner edge. We use $v_{\mathrm{diff}} \approx \eta/\beta h$ (h is the initial disk scale height and depends on R_{d}), which differs from GW's approximation by the factor β. This factor is necessary because the average disk scale height during the simulations is larger than the initial value. This has two causes: a) the magnetic interaction increases the scale height above the initial analytical value, and b) the numerical diffusion of disk material is not negligible (h is typically only a few grid points at R_{d}). For each case, then, we used our explit value of $\eta = 10^{17}$ cm^2 s^{-1}, and chose β to best fit the disk oscillation period. In all

cases, β ranged from 3 to 9.

The predictions of the modified model presented here (triangles in fig.'s 11 and 12) match the simulated results (squares) well for the cases with various stellar magnetic field strengths and disk densities, but are consistently too small for the cases with various field topologies. Remember that the the cases in panel c) of figures 11 and 12 have a disk which is initially truncated further out than all other cases. Since their initial truncation radius is further out than the final disk oscillation amplitude of the weak field case (to which they are otherwise similar), these cases have an initial state in which $\dot{M}_{\mathrm{inner}} < \dot{M}_{\mathrm{outer}}$. The mismatch between the data an predictions for these models may be due to a significant alteration of the disk density profile from its initial state.

The agreement of the predictions of this modified model with the data implies that the fundamental assumptions of the model are valid (at least in the simulations). Those assumptions are: 1) The disk oscillations are associated with a flux interchange process where magnetic flux diffuses into the inner-most edge of the disk. 2) The disk oscillations are driven by spin-down torques associated with the magnetic field that threads the disk. 3) The spin-down rate is driven by the surface density of the accretion disk and the magnetic field topology. 4) What appear to be large scale disk oscillation are actually the spin-down of a ring of material from the inner most edge of the disk.

4. Summary and Discussion

The mechanism presented by GBW and GW for the launching of jets is promising, but it is difficult to make a priori predictions, given the large number of parameters in the star-disk system. One has to consider the effects of the mass of the star and disk, the magnetic field strength, and the stellar rotation rate, to name a few. In addition, the disk responds to the conditions in its environment, so one must also consider the self-consistent interaction between the disk, outflow, and changing magnetic field topology. The complexity of this model prompted us to carry out a parameter survey using magnetohydrodynamic simulations. Using the case presented by GBW as a baseline, we examined cases with various initial disk densities, various stellar dipole field strengths, and cases with additional "primordial" field associated with the disk. The results of this survey are:

1. The fundamental mechanism for jet formation is robust.

2. The star-disk-outflow system is self-regulating.

3. The mechanism is independent of magnetic flux that may exist in the disk.

4. We have improved the disk oscillation model of GW.

The robust nature of the mechanism is best demonstrated by examination of figures 1 – 3. For variations of initial disk density, variations in stellar magnetic field strength, and variations in initial disk truncation points and large scale magnetic field topologies, all of the simulations produced outflows with similar morphologies. All outflows consisted of a highly collimated, knotty jet and a less collimated "disk wind" (including a "wispy" structure associated with magnetic reconnection). Also, the outflows were always episodic with the period set by the oscillations of the inner edge of the disk. The magnitude and timescales of outflow characteristics, however, do depend on the magnetic field strength and the density of the accretion disk, and we were able to address these dependencies in a quantitative way.

As seen in figures 4 – 6, 10 – 12, and in table 3, variation of key system parameters do indeed cause variations in outflow properties, but the relationship is fairly weak (the strongest power law relating a system property to the initial conditions has $n = -0.44$). This self-regulating nature of the system suggests that the self-consistent interaction between the disk, outflow, and stellar magnetosphere "softens" the effect of any single parameter change. For example, we found in §3.1 that the large scale magnetic field structure rapidly evolves to a configuration that removes angular momentum from the disk at a rate that depends most strongly on the evolved field and much more weakly on other parameters. Also, when the stellar magnetic field is changed, the outer region of the evolved field (which is important for the extraction of angular momentum) has characteristics which only partially reflect the surface value change.

The robust and self-regulating nature of this system imply that, if such a mechanism does occur in astrophysical systems, it should indeed be ubiquitous, and may actually be the prime mechanism for the formation of non-relativistic astrophysical jets. Unfortunately the self-regulating nature also means that observable (or deduceable) properties of outflows, such as the mass outflow rate or the rate of angular momentum expelled from the system, will contain a limited amount of information about the properties of the star-disk systems.

Figures 4 – 6 and 10 – 12 also demonstrated with some certainty that the system properties examined do not depend on the amount or direction of magnetic flux that initially threads the disk. For each system property we examined, there is at least a weak dependence on the initial stellar magnetic field energy, evident in panel b) of each of these figures. However, as seen in the c) panels, for the cases with additional vertical field (and therefore additional magnetic energy in the disk), there were no convincing trends. Implicitly, therefore, it is the interaction between the stellar magnetosphere and the inner edge of the accretion disk that drives the outflow, as opposed to the existence (via artificial initial conditions) of a dipole field that threads the disk everywhere at $t = 0$. Note, however, that for

stronger vertical fields, magnetocentrifugal launching of disk plasma may increase at larger radii (leading to an increased collimation of the material launched from the disk inner edge). Magnetized disk models (e.g., Pudritz & Ouyed 1997; Camenzind 1997; Kuwabara et al. 2000) will become important, independent from and in addition to the mechanism presented here. A system with a dynamically important stellar dipole field and disk-associated field might produce an outflow with an episodic/unsteady core (closest to the axis of rotation) and a "cocoon" of material originating from the disk.

We also evaluated and modified the disk oscillations model of GW (§3). Using a semi-analytical method, we tested and confirmed many of their basic assumptions, including the idea that the oscillation period is set by spin down time of disk inner edge, not by the inflation of magnetosphere. Therefore, we demonstrated that the basic physical mechanism for disk oscillations is understood.

There is still work to be done with the accretion/ejection mechanism presented here in order to decide whether such a process occurs in real astrophysical systems. Future work is planned to determine the importance of other properties of the system, though the qualitative mechanism is valid for a wide range of parameters. In particular, the stellar rotation rate certainly influences the details of the outflow characteristics, but the inflation of the magnetosphere will always occur, even in the extreme case of a non-rotating star, due to the differential rotation in the accretion disk. Also, a more realistic treatment of the accretion disk, possibly including the effects of the disk viscosity or the magnetorotational instability (Balbus & Hawley 1991), would affect the star-disk interaction through the accretion rate ($\dot{M}_{\mathrm{outer}}$), and will thus change the period and amplitude of the disk oscillations. Future work will also examine the system under true three-dimensional conditions. The effect of radiative cooling/heating may not be negligible, especially considering that the coupling of the field to the gas is dependent on the specific ionization state and composition of the circumstellar matter.

The disk oscillation process, and therefore the jet launching mechanism, is fundamentally driven by a diffusive process which is poorly understood. Recall that the mechanism requires magnetic reconnection (a diffusive process with physics that are partially understood; see Priest & Forbes 2000) for accretion and re-expansion. GBW point out that this model is not particular sensitive to the physics of magnetic reconnection, since regions of oppositely directed magnetic field are driven together by the disk oscillations. However, this is only a partial solution to the dilemma, since the disk oscillation mechanism itself is initiated by the diffusion of stellar magnetospheric flux into the disk inner edge.

The timescale for knot formation predicted by this mechanism is a factor of ~ 15 different than observed for HH 30, and the rudimentary scaling laws offered by this parametric

study do not offer an obvious solution to the discrepancy. The timescale predicted by this work (several tens of days) cannot presently be resolved by direct imaging (there would be several tens of knots in a typical optical resolution element), so one cannot yet rule it out. However, even if there exists a short timescale present in astrophysical systems that can be explained by this mechanism, there is then no detailed theoretical prediction of the observed longer timescale. A primary focus of future work with this model will be the timescale for disk oscillations/knot formation.

Another criticism of this work (as well as many other models; see §1) addresses the assumption that the central star has a strong dipole magnetic field (dominating over other multipolar components which may exist). Detailed observations of the magnetic fields in T Tauri stars (see, e.g., Safier 1998; Johns-Krull et al. 1999) suggest that strong, ordered fields may not dominate; rather, the stellar field topology appears to be time-variable and non-axisymmetric. Whether such a field can participate in the mechanism described here (e.g., via non-axisymmetric magnetic flux tubes connecting the star and disk) is not known.

REFERENCES

Bacciotti, F. 1997, in IAU Symp. 182: Herbig-Haro Flows and the Birth of Stars, Vol. 182, 73

Bacciotti, F., Mundt, R., Ray, T. P., Eislöffel, J., Solf, J., & Camezind, M. 2000, ApJ, 537, L49

Balbus, S. A., & Hawley, J. F. 1991, ApJ, 376, 214

Blandford, R. D., & Payne, D. G. 1982, MNRAS, 199, 883

Bouvier, J., Bertout, C., Benz, W., & Mayor, M. 1986, A&A, 165, 110

Burrows, C. J., et al. 1996, ApJ, 473, 437

Camenzind, M. 1997, in IAU Symp. 182: Herbig-Haro Flows and the Birth of Stars, ed. B. Reipurth & C. Bertout (Dordrecht: Kluwer), 241

Eislöffel, J., Mundt, R., Ray, T. P., & Rodriguez, L. F. 2000, in Protostars and Planets IV, ed. V. Mannings, A. P. Boss, & S. S. Russell (Tucson: Univ. of Arizona Press), 815

Frank, A., & Mellema, G. 1996, ApJ, 472, 684

Goodson, A. P., Böhm, K., & Winglee, R. M. 1999, ApJ, 524, 142

Goodson, A. P., & Winglee, R. M. 1999, ApJ, 524, 159

Goodson, A. P., Winglee, R. M., & Böhm, K. H. 1997, ApJ, 489, 199

Hartmann, L. 1997, in IAU Symp. 182: Herbig-Haro Flows and the Birth of Stars, ed. B. Reipurth & C. Bertout (Dordrecht: Kluwer), 391

Hayashi, M. R., Shibata, K., & Matsumoto, R. 1996, ApJ, 468, L37

Hirth, G. A., Mundt, R., & Solf, J. 1997, A&AS, 126, 437

Johns-Krull, C. M., Valenti, J. A., Hatzes, A. P., & Kanaan, A. 1999, ApJ, 510, L41

Königl, A. 1982, ApJ, 261, 115

Königl, A., & Pudritz, R. E. 2000, in Protostars and Planets IV, ed. V. Mannings, A. P. Boss, & S. S. Russell (Tucson: Univ. of Arizona Press), 759

Kuwabara, T., Shibata, K., Kudoh, T., & Matsumoto, R. 2000, PASJ, 52, 1109

Kwan, J., & Tademaru, E. 1988, ApJ, 332, L41

Kwan, J., & Tademaru, E. 1995, ApJ, 454, 382

Lovelace, R. V. E., Romanova, M. M., & Bisnovatyi-Kogan, G. S. 1995, MNRAS, 275, 244

Lovelace, R. V. E., Romanova, M. M., & Bisnovatyi-Kogan, G. S. 1999, ApJ, 514, 368

Michel, F. C. 1969, ApJ, 158, 727

Miller, K. A., & Stone, J. M. 1997, ApJ, 489, 890

Priest, E., & Forbes, T. 2000, Magnetic reconnection : MHD theory and applications (Cambridge U. P.)

Pudritz, R. E., & Ouyed, R. 1997, in IAU Symp. 182: Herbig-Haro Flows and the Birth of Stars, ed. B. Reipurth & C. Bertout (Dordrecht: Kluwer), 259

Raga, A. C., Böhm, K.-H., & Cantó, J. 1996, RMxAA, 32, 161

Reipurth, B., & Bally, J. 2001, ARA&A, 39, 403

Reipurth, B., Raga, A. C., & Heathcote, S. 1992, ApJ, 392, 145

Richtmyer, R. D., & Morton, K. W. 1967, Difference Methods for Initial-Value Problems
        (New York, NY: Wiley-Interscience)

Safier, P. N. 1998, ApJ, 494, 336

Shakura, N. I., & Sunyaev, R. A. 1973, A&A, 24, 337

Solf, J. 1989, in Low Mass Star Formation and Pre-main Sequence Objects, ed. B. Reipurth
        (Garching: ESO), 399

Solf, J. 1997, in IAU Symp. 182: Herbig-Haro Flows and the Birth of Stars, ed. B. Reipurth
        & C. Bertout (Dordrecht: Kluwer), 63

Solf, J., & Böhm, K. H. 1993, ApJ, 410, L31

Uzdensky, D. 2002, submitted to ApJ

Weber, E. J., & Davis, L. J. 1967, ApJ, 148, 217
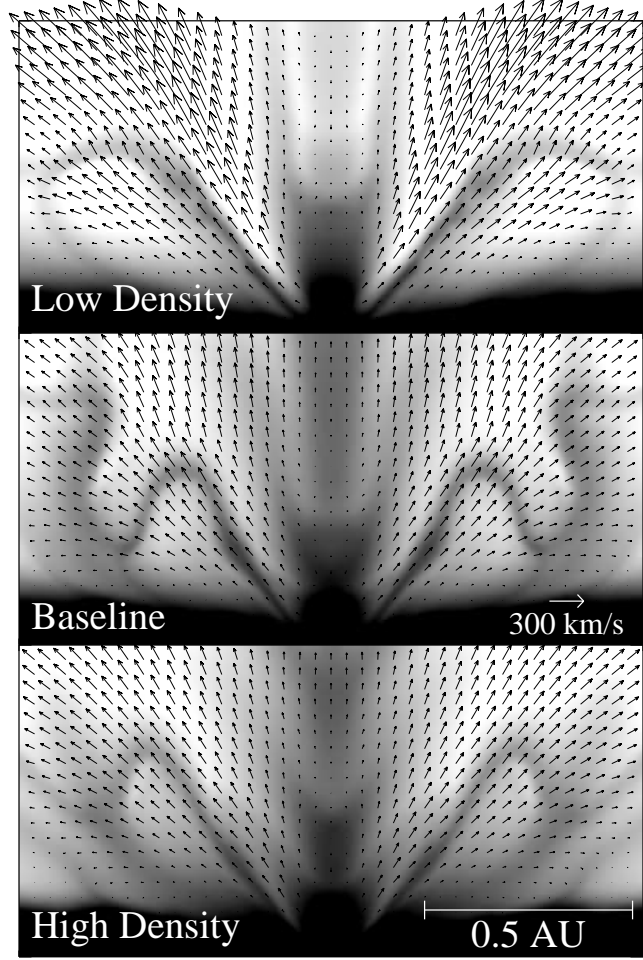
Fig. 1.— A snapshot of density and poloidal velocity vectors illustrates the jet and disk wind for all cases of disk density variation. Grayscale ($\log n \leq 10^{-20.7}$, for n in cm^{-3}, is white and $\geq 10^{-18.5}$ is black) and velocity scale is consistent for all frames. The panels, from top to bottom, are the low density case (at $t = 147$ days), the baseline case (at $t = 136^{\mathrm{d}}$), and the high density case (at $t = 137^{\mathrm{d}}$). In each panel, the equatorial plane is along the bottom, and the star is at bottom center.
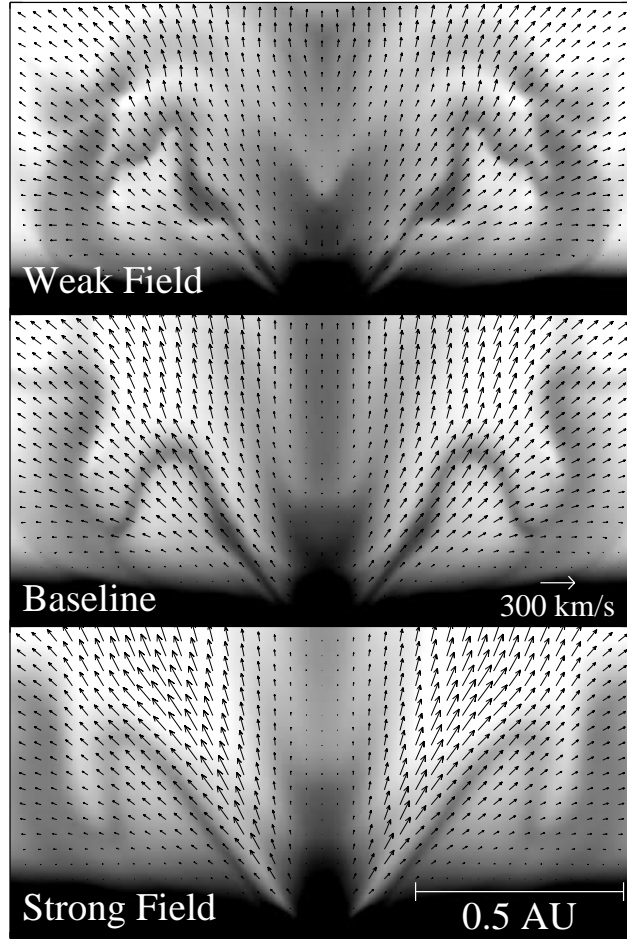
Fig. 2.— Same as figure 1 but for weak field (at $t = 137^{\mathrm{d}}$), baseline (at $t = 136^{\mathrm{d}}$), and strong field (at $t = 129^{\mathrm{d}}$) cases.
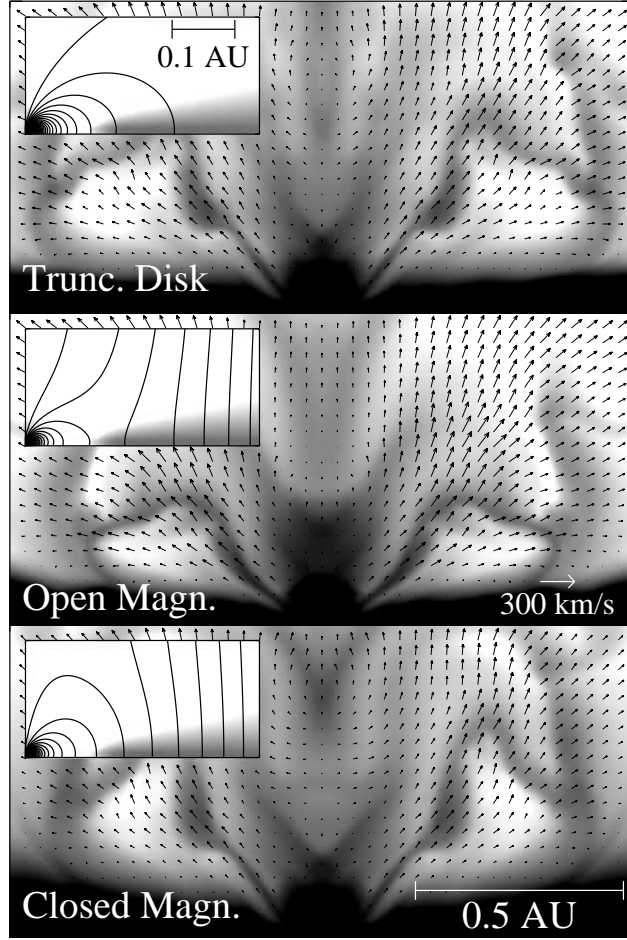
Fig. 3.— Same as figure 1 but for truncated disk (at $t = 143^{\rm d}$), open magnetosphere (at $t = 138^{\rm d}$), and closed magnetosphere cases (at $t = 145^{\rm d}$). The insets in each panel show the magnetic field topologies at the start of the simulation (at a smaller scale; star is at lower left).
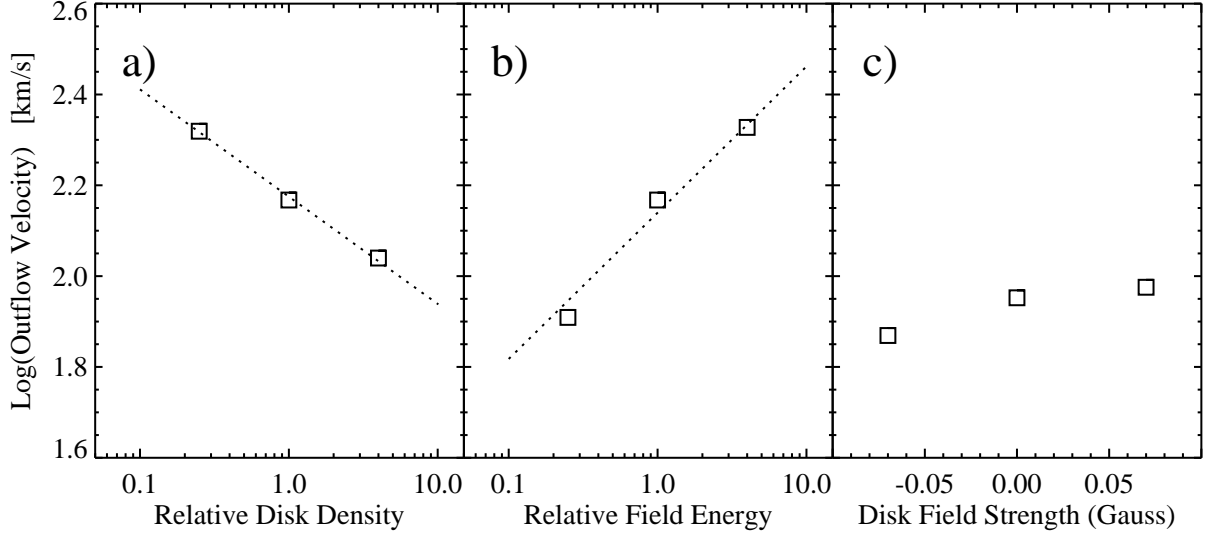
Fig. 4.— The maximum radial outflow velocities (see text for details), for all cases, reveal a dependence on system parameters. The panels show variation with respect to a) disk density, b) stellar magnetic field energy, and c) the strength of a vertical magnetic field (in addition to the stellar dipole field). The abscissa values in panels a) and b) are relative to the baseline case. The dotted lines are power law fits to the data.
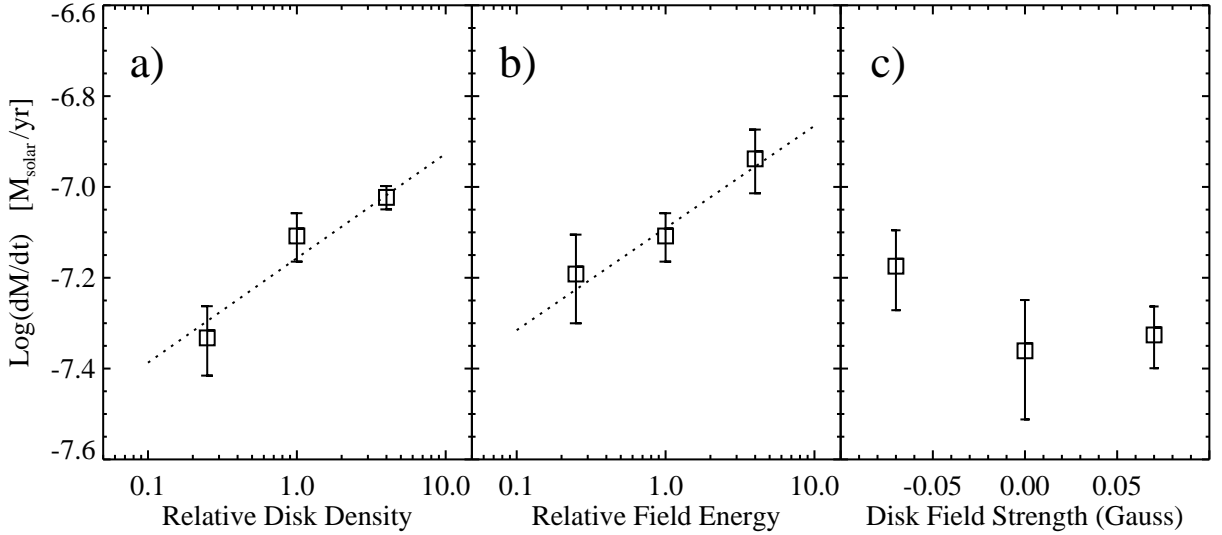
Fig. 5.— Similar to figure 4 but for mass outflow rates, $\dot{M}_w$.
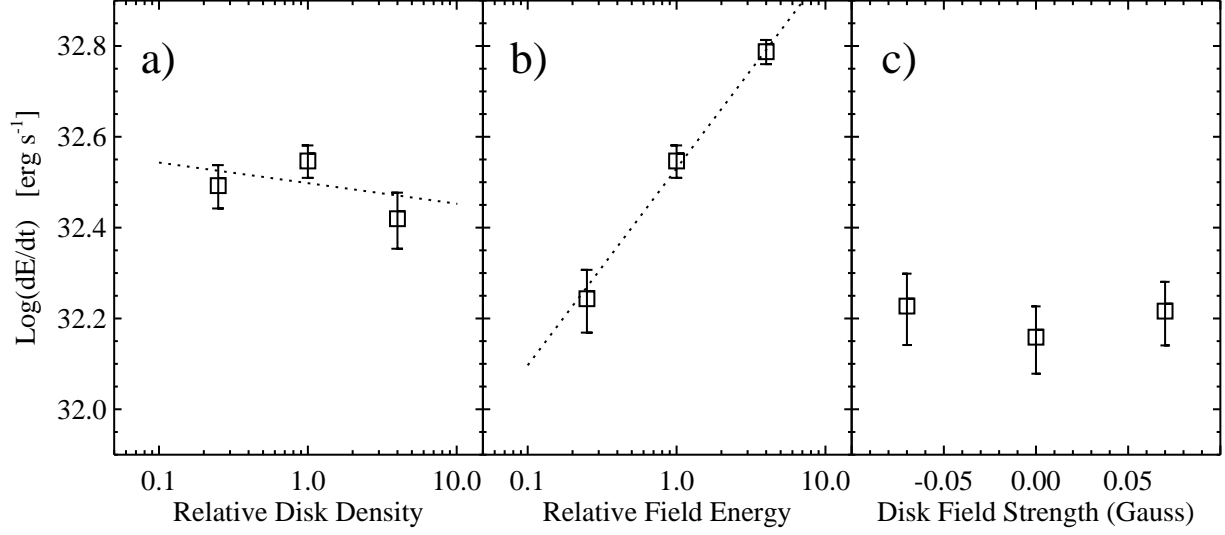
Fig. 6.— Similar to figure 4 but for outflow luminosity, $L_{\rm w}$ (see text).

Table 1.   Case matrix for parametric study.

Case Name	Variation	Physical Parm.	Comments
Baseline	None	N/A	See GBW
Low Density	$\rho_{\rm disk} \div 4.0$	$\rho_{\rm mid}^a = 0.55$	$\cdots$
High Density	$\rho_{\rm disk} \times 4.0$	$\rho_{\rm mid}^a = 8.83$	$\cdots$
Weak Field	$B_* \div 2.0$	$B_*({\rm pole}) = 900$ G	$\cdots$
Strong Field	$B_* \times 2.0$	$B_*({\rm pole}) = 3600$ G	$\cdots$
Truncated Disk	Disk at 19 R_*	N/A	Applied to weak field case
Closed Magn.	Vertical field closes magnetosphere	Primordial field of 0.07 G in $-z$ direction	Used for Truncated disk case only
Open Magn.	Vertical field opens magnetosphere	Primordial field of 0.07 G in $+z$ direction	As above but oppositely directed primordial field

^{a} $\rho_{\rm mid}$ is the mass density in the disk midplane at 10 $R_\odot$ in units of 10^{-10} g cm^{-3}.
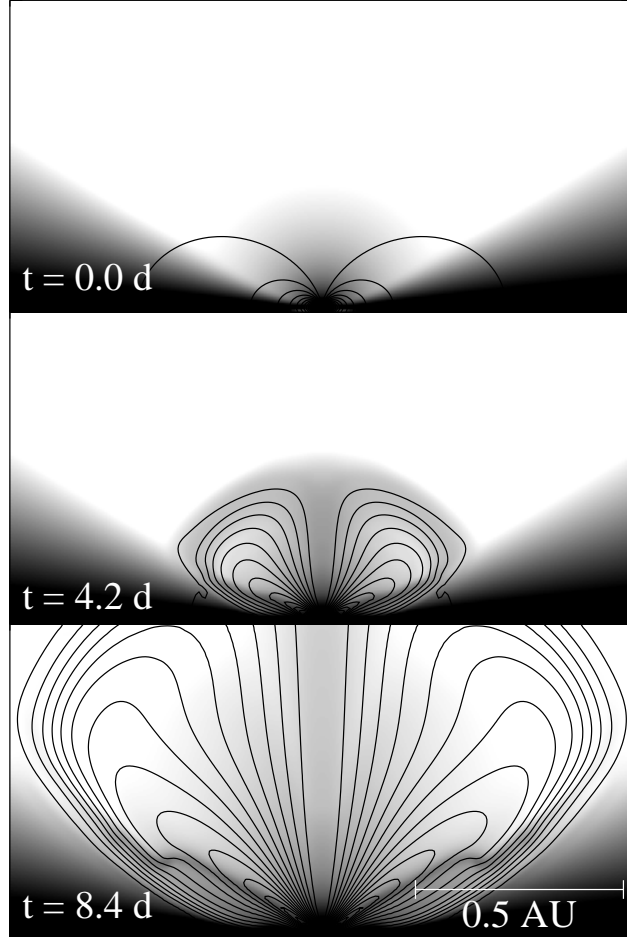
Fig. 7.— Snapshots from different times, early in the evolution of the baseline case, illustrate the rapid expansion of the poloidal magnetic field (solid lines). The grayscale is $\log n$ ($\leq 10^{-22}$ is white and $\geq 10^{-17.5}$ is black, for n in cm^{-3}).
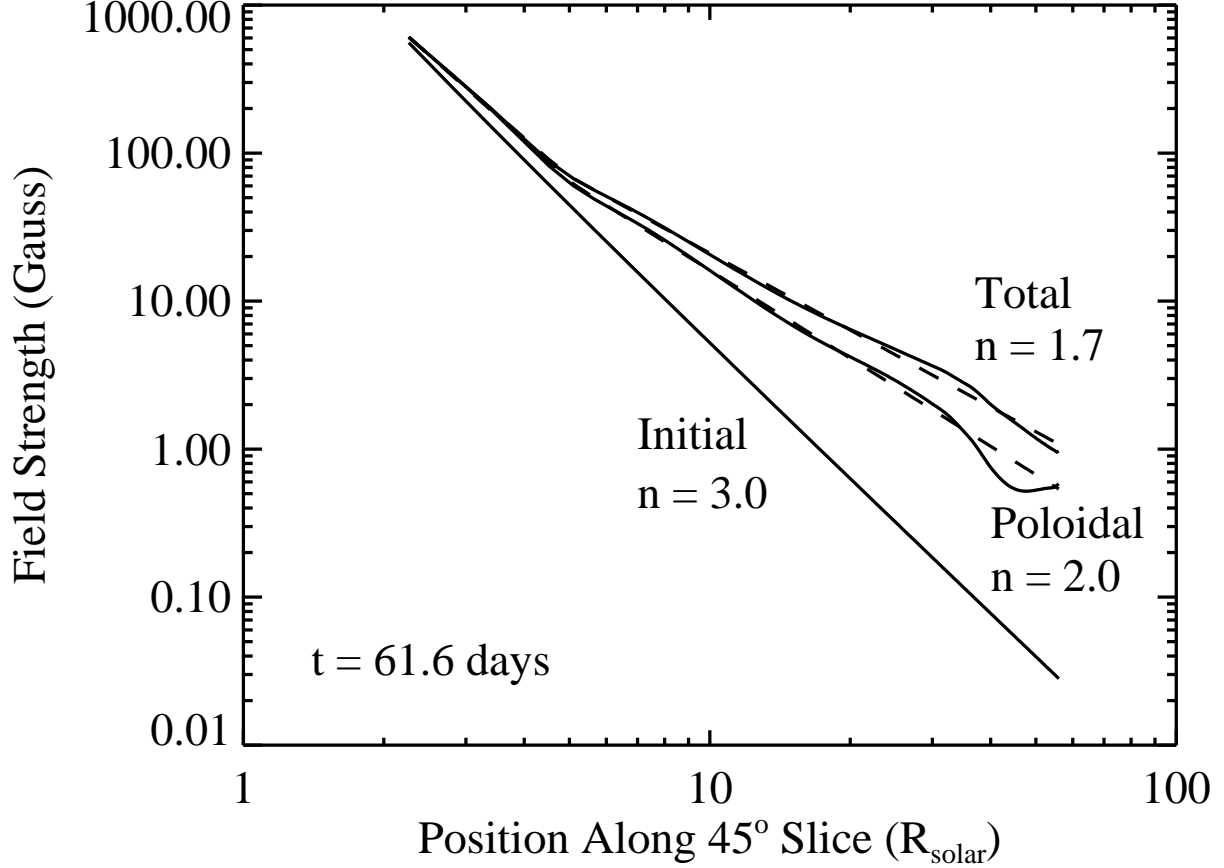
Fig. 8.— The magnetic field strength as a function of distance from the central star (along a 45 degree line in the meridional plane) quantifies the expansion of the magnetic field for the baseline case. The lower solid line is the initial dipole field, the top solid line is the strength of the evolved total magnetic field at $t = 61.6$ days, and the middle solid line is the poloidal field at the same time. Dashed lines are broken power law fits to the data, and the power, n, in the exterior region of the fit is shown.
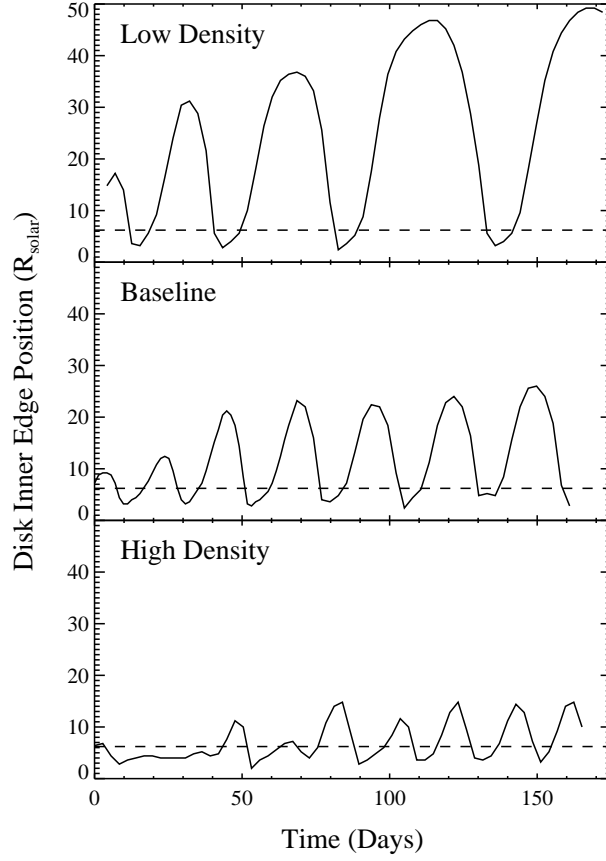
Fig. 9.— The radial location of the inner edge of the accretion disk as a function of time (solid line) is sensitive to variations in the disk mass. The three panels correspond to three cases with different initial disk densities, and the dashed line in each is the location of the Keplerian co-rotation point.
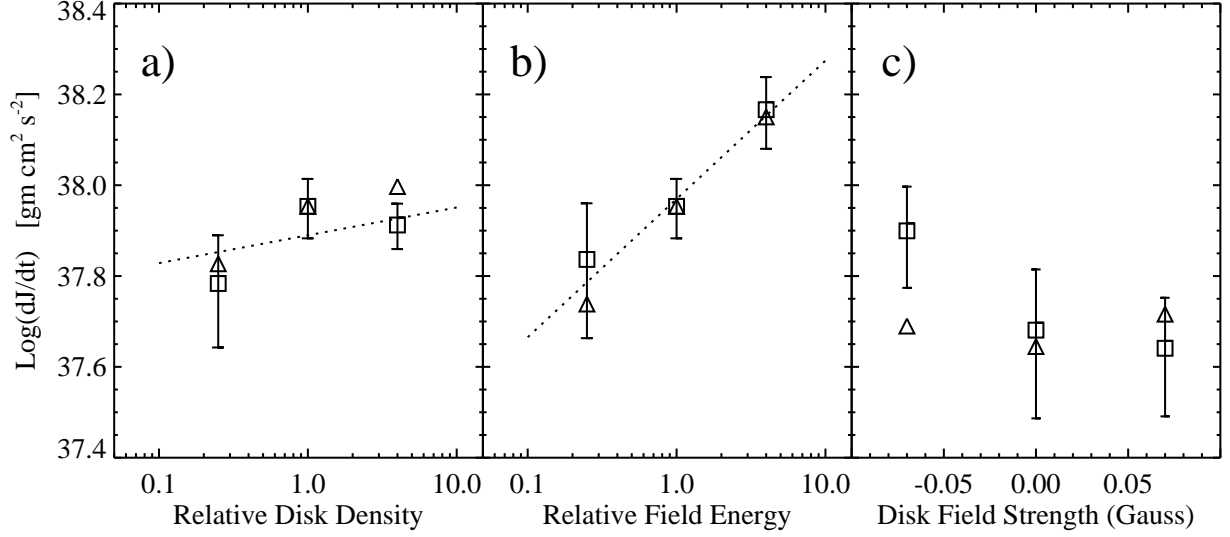
Fig. 10.— The squares and dotted lines are as in figure 4 but for angular momentum carried in the outflow, $\dot{J}_\mathrm{w}$. The triangles represent a semi-analytical calculation for each case (see text).
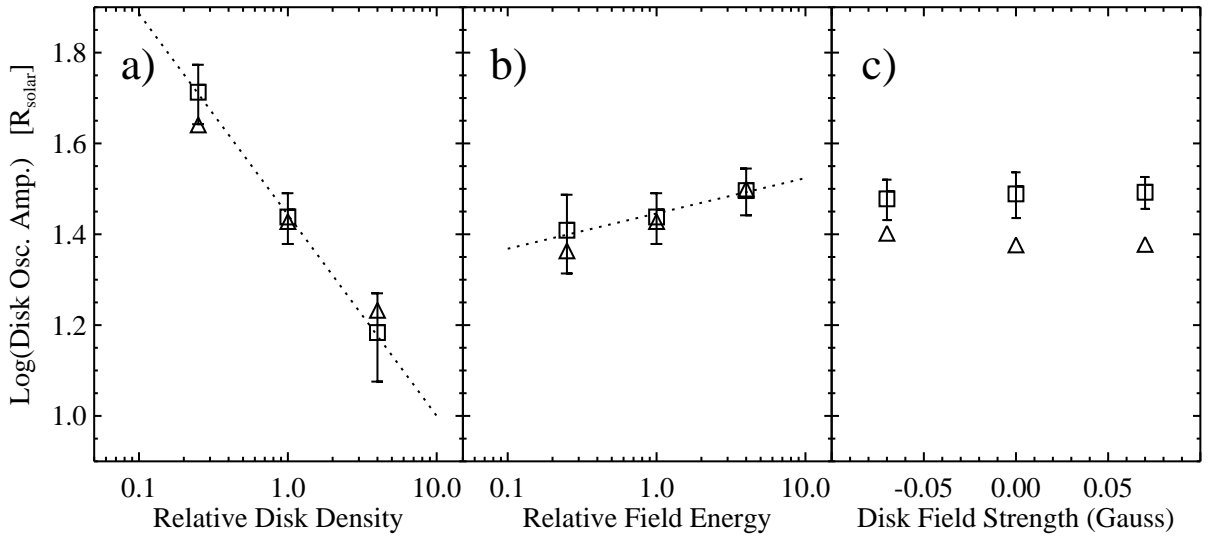

Fig. 11.— The squares and dotted lines are as in figure 4 but for disk oscillation amplitudes at $t = 160$ days. The triangles represent a semi-analytical calculation (see text).
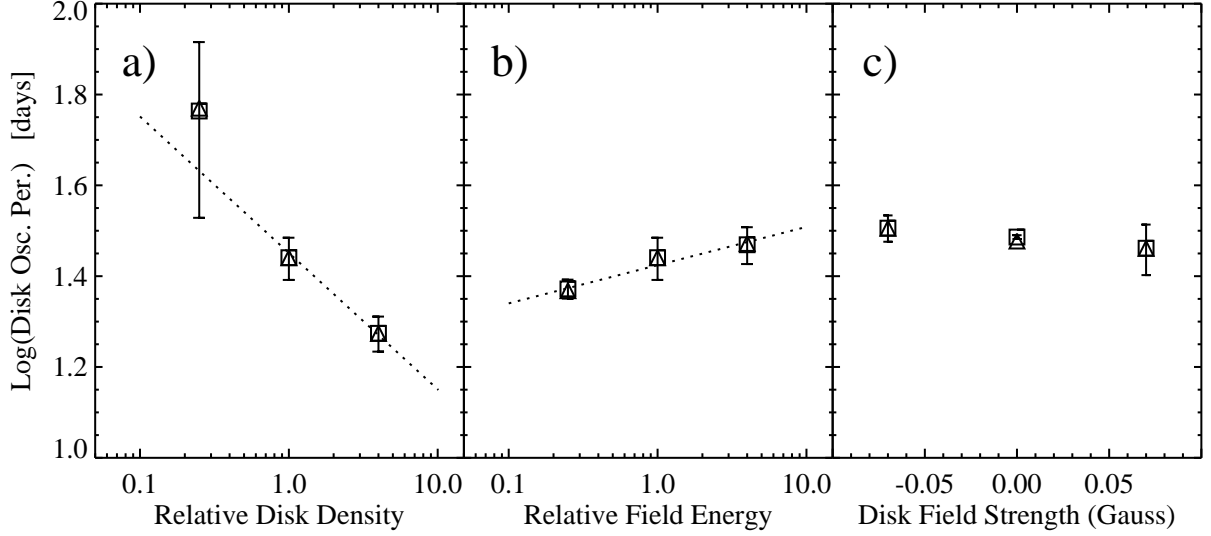
Fig. 12.— The squares and dotted lines are as in figure 4 but for disk oscillation period at t = 160 days. The triangles represent a semi-analytical calculation (see text).

Table 2.   Fit parameters of large scale magnetic field strength.

Case	B_{01}^a	n_1	$B_{02}(\text{tot})^a$	$n_2(\text{tot})$	$B_{02}(\text{pol})^a$	$n_2(\text{pol})$
Baseline	2010 ± 10	2.98 ± 0.02	750 ± 10	1.76 ± 0.01	840 ± 20	1.94 ± 0.01
Low Dens.	1890 ± 20	2.82 ± 0.04	900 ± 30	1.88 ± 0.02	960 ± 30	1.98 ± 0.02
High Dens.	1930 ± 10	2.92 ± 0.01	760 ± 10	1.75 ± 0.01	940 ± 30	2.01 ± 0.02
Weak Field	1050 ± 10	2.89 ± 0.01	550 ± 10	1.71 ± 0.01	580 ± 20	1.88 ± 0.03
Strong Field	3800 ± 10	2.94 ± 0.01	1180 ± 10	1.83 ± 0.01	1450 ± 40	2.01 ± 0.02
Trunc. Disk	1090 ± 10	2.89 ± 0.01	550 ± 20	1.74 ± 0.01	560 ± 10	1.85 ± 0.02
Closed Magn.	1100 ± 10	2.90 ± 0.02	550 ± 10	1.73 ± 0.01	570 ± 10	1.88 ± 0.02
Open Magn.	1100 ± 10	2.87 ± 0.02	550 ± 10	1.71 ± 0.01	560 ± 10	1.82 ± 0.02

[a] in Gauss

Table 3.   Summary of dependences.

Outflow Property	Disk Density	Initial Dipole Magnetic Energy
Wind Morphology	Independent	Independent
Outflow Velocity	-0.24	0.32
$\dot{M}_{\mathrm{w}}$	0.23 ± 0.06	0.22 ± 0.10
L_{w}	-0.05 ± 0.06	0.43 ± 0.04
$\dot{J}_{\mathrm{w}}$	0.06 ± 0.07	0.30 ± 0.12
Period[a]	-0.30 ± 0.05	0.08 ± 0.02
Amplitude[a]	-0.44 ± 0.09	0.08 ± 0.08

[a] Refers to the oscillations of the disk inner edge, which drive oscillations in the outflow.